Journal of Energy Chemistry 85 (2023) 144–153

Contents lists available at ScienceDirect

Journal of Energy Chemistry

journal homepage: www.elsevier.com/locate/jechem

http://www.journals.elsevier.com/journal-of-energy-chemistry/

Unexpected Li displacement and suppressed phase transition enabling highly stabilized oxygen redox in P3-type Na layered oxide cathode

Myungeun Choi [a,b,1], Hobin Ahn [a,b,1], Hyunyoung Park [a,b], Yongseok Lee [a,b], Jinho Ahn [a,b], Bonyoung Ku [a,b], Junseong Kim [a,b], Wonseok Ko [a,b], Jungmin Kang [a,b], Jung-Keun Yoo [c], Duho Kim [d,e,*], Jongsoon Kim [a,b,*]

[a] Department of Energy Science, Sungkyunkwan University, Suwon 16419, Republic of Korea
[b] SKKU Institute of Energy Science and Technology (SIEST), Sungkyunkwan University, Suwon 16419, Republic of Korea
[c] Carbon Composites Department, Korea Institute of Materials Science (KIMS), Changwon 51508, Republic of Korea
[d] Department of Mechanical Engineering (Integrated Engineering Program), Kyung Hee University, 1732, Deogyeong-daero, Giheung-gu, Yongin-si, Gyeonggi-do 17104, Republic of Korea
[e] Department of KHU-KIST Convergence Science and Technology, Kyung Hee University, 23, Kyunghee-daero Dongdaemun-gu, Seoul 02447, Republic of Korea

ARTICLE INFO

Article history:
Received 26 April 2023
Revised 7 June 2023
Accepted 10 June 2023
Available online 22 June 2023

Keywords:
Layered oxide cathode
Oxygen redox reaction
Structural stability
Li displacement
No phase transition

ABSTRACT

Oxygen redox is considered a new paradigm for increasing the practical capacity and energy density of the layered oxide cathodes for Na-ion batteries. However, severe local structural changes and phase transitions during anionic redox reactions lead to poor electrochemical performance with sluggish kinetics. Here, we propose a synergy of Li-Cu cations in harnessing the full potential of oxygen redox, through Li displacement and suppressed phase transition in P3-type layered oxide cathode. P3-type $Na_{0.7}[Li_{0.1}Cu_{0.2}Mn_{0.7}]O_2$ cathode delivers a large specific capacity of ~212 mA h g^{-1} at 15 mA g^{-1}. The discharge capacity is maintained up to ~90% of the initial capacity after 100 cycles, with stable occurrence of the oxygen redox in the high-voltage region. Through advanced experimental analyses and first-principles calculations, it is confirmed that a stepwise redox reaction based on Cu and O ions occurs for the charge-compensation mechanism upon charging. Based on a concrete understanding of the reaction mechanism, the Li displacement by the synergy of Li-Cu cations plays a crucial role in suppressing the structural change of the P3-type layered material under the oxygen redox reaction, and it is expected to be an effective strategy for stabilizing the oxygen redox in the layered oxides of Na-ion batteries.

1. Introduction

Because of the limited and concentrated Li sources on Earth, the high production cost of lithium-ion batteries (LIBs) is one of the main problems preventing their further application, and it is difficult to meet the growing demands [1–5]. Accordingly, many researchers have studied the development of low-cost alternatives to LIBs [6–10]. Recently, sodium-ion batteries (SIBs) have been considered as one of the most promising alternatives because of the following advantages: (1) low production costs owing to unlimited Na resources in the sea; (2) alkali-ion-based reaction mechanisms similar to those of LIBs [11–13]. Among the various cathodes for SIBs, layered oxides, $Na_x[TM]O_2$ (TM = transition metals), have been extensively investigated because of their large gravimetric capacities [14–17]. Unfortunately, the intrinsically low energy density of Na-based cathodes still poses a challenge for enabling practical energy storage systems instead of LIBs. In light of this barrier, inspired by the in-depth understanding of the reaction mechanism of Li_2MnO_3 for LIBs [18], oxygen redox (OR) was assigned as a new paradigm to overcome the energy density limitation in SIBs because of the high redox potential above 4.0 V versus that of Na^+/Na [19–23]. In experimental and computational analyses, the OR during Na^+ de/intercalation was demonstrated based on Li-incorporated prismatic-type (P-type) Mn layered oxides featuring Mn^{4+} ions that are not straightforward to further oxidize to their higher valence state but trigger the undesired structural change under phase transition from P- to octahedral-type (O-type) structure upon (dis)charging [24]. This unwanted variation has been acknowledged as a critical reason

* Corresponding authors.
E-mail addresses: duhokim@khu.ac.kr (D. Kim), jongsoonkim@skku.edu (J. Kim).
[1] These authors contributed equally to this work.

https://doi.org/10.1016/j.jechem.2023.06.009

for the poor electrochemical performance of P-type OR cathodes [25,26].

Intriguingly, the Li ions in the TM layer for the OR-based Mn oxides were studied in depth to unlock their important role in enabling the reversibility of anionic redox, and their movement upon charging and discharging was observed over the crystal framework [22,27–29]. In addition, delivering a large oxygen capacity triggers the formation of O—O dimers, degrading the electrochemical activity [30,31]. Huang and coworkers reported the Li-substituted P3-type oxide cathode with OR reversibility and suggested that Li in the P3-$Na_{0.6}[Li_{0.2}Mn_{0.8}]O_2$ might suppress the irreversible transformation of the oxidized oxygen ions, despite experiencing severe capacity retention [32]. Therefore, modulating the oxygen capacity led to a rational approach from a practical point of view, and this concept was confirmed by redox-active cations incorporated into various oxide models before their anionic redox. Recently, Armstrong and coworkers suggested that P3-$Na_{0.67}[Cu_{0.1}Mn_{0.9}]O_2$, doped with high-electronegativity Cu^{2+}, exhibited a strong Cu—O covalency, facilitating the OR activities and stabilizing the adjacent oxygen ions [33,34].

These considerations motivated us to induce the synergetic effect of cations to harness the full potential of the OR in SIBs. Therefore, in this study, Li displacement and suppressed phase transition (P3-O3″) are proposed to understand the superior electrochemical performance of the P3-type $Na_{0.7}[Li_{0.1}Cu_{0.2}Mn_{0.7}]O_2$ (P3-NLCMO) cathode with the stable OR. Theoretical calculations and advanced X-ray absorption techniques elucidate Cu-based cationic and subsequent oxygen oxidation upon charging, which reinforces the former concept. Formation energy and *operando* X-ray diffraction (XRD) results showed that there is no phase transition to the O-type structure during the OR, which were intriguingly correlated with Li displacement in the local structure point of view. Based on a concrete understanding of the reaction mechanism of the P3-type model, the cooperating effect provides a practical strategy for exploiting the OR in layered oxide cathodes, and we believe that this concept is universal for developing SIBs.

2. Experimental

2.1. Synthesis of P3-$Na_{0.7}[Li_{0.1}Cu_{0.2}Mn_{0.7}]O_2$

To synthesize P3-$Na_{0.7}[Li_{0.1}Cu_{0.2}Mn_{0.7}]O_2$, Na_2CO_3 (Alfa, 99.5%), Li_2CO_3 (Alfa, 99.5%), Mn_2O_3 (Alfa, 99.9%), and CuO (Samchun, 98%) were used as precursors. Also, P3-$Na_{0.7}[Li_{0.2}Cu_{0.1}Mn_{0.7}]O_2$ was synthesized using Na_2CO_3 (Alfa, 99.5%), Li_2CO_3 (Alfa, 99.5%), $MnCO_3$ (Sigma-Aldrich, 99%), and CuO (Samchun, 98%) as precursors. An excess of Na_2CO_3 (Alfa, 99.5%, 5 wt% excess) and Li_2CO_3 (Alfa, 99.5%, 5 wt% excess) were added to compensate for the loss of Na and Li at high temperatures. Stoichiometric amounts of the precursors were obtained using high-energy ball milling at 400 r min^{-1} for 12 h. The powders were sealed in an Ar-filled glove box to prevent oxygen and water pollutants. Then, the mixed powders were pelletized and heated at 625 ℃ for 12 h (heating rate of 2.5 ℃ min^{-1}) in air. After calcination, the obtained samples were cooled in a tube furnace without limiting the cooling rate.

2.2. Materials characterization

The crystal structures of P3-$Na_{0.7}[Li_{0.1}Cu_{0.2}Mn_{0.7}]O_2$ and P3-$Na_{0.7}[Li_{0.2}Cu_{0.1}Mn_{0.7}]O_2$ were analyzed using X-ray diffraction (XRD, PANalytical Empyrean) with Mo K_α radiation (λ = 0.70932 Å) in the 2θ range between 4.61° and 34.32° with a step size of 0.01°. And then, the angles of XRD patterns were converted with Cu K_α radiation (λ = 1.54178 Å) in order to compare with other studies. Rietveld refinement was conducted using the FullProf software based on the obtained XRD data [35]. *Operando* XRD (*o*-XRD) patterns of P3-$Na_{0.7}[Li_{0.1}Cu_{0.2}Mn_{0.7}]O_2$ were obtained during charge/discharge at a current density of 15 mA g^{-1} within the voltage range of 1.5–4.5 V (vs. Na^+/Na). To investigate the particle morphology and microstructure of $Na_{0.7}[Li_{0.1}Cu_{0.2}Mn_{0.7}]O_2$, field-emission scanning electron microscopy (FE-SEM; HITACH S4700) was used at the Cooperative Center for Research Facilities (CCRF) at Sungkyunkwan University. Field-emission transmission electron microscopy (FE-TEM; JEM-F200), d-space with selected area electron diffraction (SAED) patterns, and transmission electron microscopy-energy-dispersive X-ray spectroscopy (TEM-EDS) were performed at the National Center for Inter-University Research Facilities (NCIRF) at Seoul National University. Each sample image was recorded using a 4 k × 4 k CCD camera (Gatan Oneview 1095). Before the measurements, all samples were dispersed in ethanol using an ultrasonicator and sprayed dropwise onto a carbon-coated Cu TEM grid. Subsequently, the samples were dried at room temperature overnight to evaporate ethanol. The atomic ratio of Na, Li, Cu and Mn was determined using inductively coupled plasma atomic emission spectrometry (ICP-AES; OPTIMA 8300, Perkin-Elmer) at the National Center for Inter-University Research Facilities (NCIRF) at Seoul National University. The valence states of Cu and Mn in the $Na_{0.7}[Li_{0.1}Cu_{0.2}Mn_{0.7}]O_2$ structure were determined using ex-situ X-ray absorption spectroscopy (XAS) spectra at the 7D and 8C beamlines at the Pohang Accelerator Laboratory (PAL); Cu and Mn metal foils were used as reference spectra. The Cu and Mn K-edge spectra were collected in transmission mode with an electron energy of 2.5 GeV and 200 mA of the current condition. The spectra contain the X-ray absorption near edge structure (XANES) and extended X-ray absorption fine structure (EXAFS) regions. The normalized XAS spectra were calibrated using linear regression to fit the pre-edge region and a quadratic polynomial to the post-edge region in the Athena program, using each metal foil spectrum [36]. To confirm the valence states of O, the total fluorescence yield (TFY) mode was measured using soft X-ray absorption spectroscopy (sXAS) spectra with high-energy grating (HEG) at the 4D PES beamline at PAL with a 525–560 eV photon range. X-ray photoelectron spectroscopy (XPS) measurements were performed using an AXIS SUPRA (Kratos Analytical) at the NCIRF to confirm the oxygen redox reaction. For XPS fitting, the XPSPEAK41 software was used, and all samples were calibrated at the binding energy of 284.6 eV of C 1*s* peak.

2.3. Electrochemical characterization

The P3-$Na_{0.7}[Li_{0.1}Cu_{0.2}Mn_{0.7}]O_2$ and P3-$Na_{0.7}[Li_{0.2}Cu_{0.1}Mn_{0.7}]O_2$ electrodes were generated from a slurry of 70 wt% active material, 20 wt% Super P as the conducting carbon, and 10 wt% poly(vinylidene fluoride) (PVDF) as a binder in *N*-methyl-2-pyrrolidone (NMP). The mixed slurry was applied onto Al foil and dried at 100 ℃ for 24 h in a vacuum oven. The mass loading of the active material was ~2 mg cm^{-2}. The dried electrode was electrochemically tested using CR2032-type coin cells assembled as half-cells, using Na metal as a reference/counter electrode, a separator (GF/F glass fiber filter), and an electrolyte (1 M $NaPF_6$ in propylene carbonate (PC) and fluoroethylene carbonate (FEC) in a volume ratio of 98:2) in an Ar-filled glove box in the SIB system. Galvanostatic charge/discharge tests were performed at various current densities (15, 30, 60, 100, 200, 300, 500 and 700 mA g^{-1} in the voltage range of 1.5–4.4 V (vs. Na^+/Na) using a battery charge/discharge test system (WBCS 3000, WonATech).

2.4. Computational detail

The Vienna Ab initio Simulation Package (VASP) was used to conduct all DFT calculations [37]. The projector-augmented wave

(PAW) pseudopotentials were applied with a plane-wave basis set, as implemented in the VASP [38]. The exchange–correlation functional was treated using the generalized gradient approximation (GGA) of the Perdew (Burke) Ernzerhof parameterization [39]. For DFT calculations, a 2 × 2 × 1 supercell structure of P3-$Na_{0.7}[Li_{0.1}Cu_{0.2}Mn_{0.7}]O_2$ was calculated with a 6 × 6 × 2 k-point grid. The GGA + *U* method was selected to represent the localization of d-orbitals in Mn and Cu ions with effective *U* values of 3.9 and 4.0, as applied in previous studies [40]. The Heyd-Scuseria-Ernzerhof (HSE06) equation was adopted to accurately calculate the projected density of states (pDOS) of Mn, Cu, and O ions [41]. For all calculations, a kinetic energy cutoff was set as 500 eV, and the structure optimization was converged until the force in the unit cell drops within 0.03 eV $Å^{-1}$ between each calculation step. The Na^+/Vacancy configurations for each composition were generated using the cluster-assisted statistical mechanics (CASM) software [42]. DFT calculations were performed for the sorted configurations with the lowest 20 electrostatic energies for each composition, which were used to depict the convex-hull plot of $Na_{0.7}[Li_{0.1}Cu_{0.2}Mn_{0.7}]O_2$.

3. Results and discussion

3.1. Material characterization of P3-$Na_{0.7}[Li_{0.1}Cu_{0.2}Mn_{0.7}O_2]$ (P3-NLCMO)

Using the conventional solid-state synthesis method, we prepared P3-NLCMO; the detailed synthesis process is summarized in the Experimental section. Fig. 1(a) shows the Rietveld refinement results of the XRD pattern of P3-NLCMO, verifying that the diffracted peaks of P3-NLCMO are indexed to the hexagonal P3-type phase with the *R*3*m* space group without any impurities. The lattice parameters of P3-NLCMO are *a* (=b) = 2.8929 (17) Å and c = 16.710 (3) Å, and the detailed structural information of P3-NLCMO, such as atomic coordinates, thermal factors, and occupancy, are tabulated in Table S1. The crystal structure of P3-type layered oxides is based on *R*3*m* space group, with all atoms located in the Wyckoff position of 3a [43,44]. Moreover, the low reliability factors of the Rietveld refinement (R_P = 7.69%, R_F = 6.31%, and χ^2 = 8.92%) indicates the high reliability. It was verified Li ions in P3-$Na_{0.7}[L_{0.1}Cu_{0.2}Mn_{0.7}]O_2$ exist in the transition metal site. Several previous research papers also showed that Li ions in P2-type layered oxide cathodes exist in the transition metal site rather than the Na site [45,46]. As shown in Fig. 1(b), the crystal structure of P3-NLCMO consisted of edge-shared [Li, Mn, Cu]O_6 octahedra and prismatic Na layers, forming an ABBCCA oxygen stacking sequence. The morphology of P3-NLCMO with a particle size of ~0.9 μm is confirmed by scanning electron microscopy (SEM, Fig. S1). Furthermore, the morphology and atomic distribution of P3-NLCMO are investigated using transmission electron microscopy (TEM) and elemental mapping based on energy-dispersive X-ray spectroscopy (EDS). Fig. 1(c) shows that the average particle size of P3-NLCMO is ~0.9 μm, and Na, Cu, Mn, and O are homogeneously distributed across the P3-NLCMO particles. The fast-Fourier transform (FFT) analysis is conducted on both surface and bulk region of P3-NLCMO particles to ensure the doping of Li ions in the lattice on indirect way (Fig. S2). It is verified that the slab distance of surface and bulk regions were 0.566 and 0.562 nm, respectively. This indicates that both the surface and bulk regions exhibited the identical crystallographic structure and a homogeneous dispersion of Li and Cu ions within the particle, without distinguishing between the surface and bulk areas. The selected-area diffraction patterns (SAED, Fig. 1d) confirmed that P3-NLCMO was well synthesized, with a single-crystalline structure in the presence of the (003) and (012) planes along the [$\bar{3}$00] direction. Using inductively coupled plasma-atomic emission spectroscopy (ICP-AES, Table S2), we confirmed that the atomic ratios of Na: Li: Cu: Mn in P3-NLCMO were ~0.74: ~0.10: ~0.20:0.70, and the results were in good agreement with the TEM-based EDS-mapping results. In addition, the average oxidation states of Mn and Cu cations were investigated using synchrotron-based X-ray absorption near edge spectroscopy (XANES). As shown in Fig. 1(e), the Mn K-edge XANES spectrum of P3-NLCMO is similar with that of MnO_2 rather than Mn_2O_3, which indicate that the oxidation state of Mn in P3-NLCMO is close to +4. And Fig. 1(f) shows the valence states of Cu cation in P3-NLCMO are close to +2.

3.2. Fundamental electrochemical properties of P3-$Na_{0.7}[Li_{0.1}Cu_{0.2}Mn_{0.7}O_2]$

Fig. 2(a and b) shows the charging/discharging curves of P3-NLCMO measured at the various current densities in the voltage range of 1.5–4.4 V (vs. Na^+/Na). The initial charge capacity of P3-NLCMO was ~174 mA h g^{-1}, corresponding to ~0.65 mol Na^+ deintercalation, at a current density of 15 mA g^{-1} (1 C = 268.2 mA g^{-1}). Considering that oxygen and Cu^{2+}/Cu^{3+} redox reactions dominantly occur above ~4.1 V and the voltage window of $3.0 \leq V \leq 4.0$ for similar Mn-based layered oxides in SIBs, the charging capacity implies occurrence of the Cu-based cationic redox and the OR in the P3-type layered oxide cathode. Upon discharging to 1.5 V, P3-NLCMO exhibited a large specific capacity of ~212 mA h g^{-1}, with an average operation voltage of ~2.73 V, indicating that a total of ~ 0.80 mol Na^+ can be reversibly de/intercalated from the host material during the charge/discharge process by not only the combined redox mechanism but also the Mn^{3+}/Mn^{4+} redox in the low-voltage region. For better understanding, we examined the differential capacity versus voltage (d*Q*/d*V*) curves of the initial charge/discharge profile of the layered cathode, as shown in Fig. S3. The results clearly confirmed that P3-NLCMO undergoes the various redox reactions of Cu, Mn and O during charge/discharge. Furthermore, the cathode showed outstanding power capability and cycle performance of P3-NLCMO, as shown in Fig. 2(b). In detail, the specific capacity of P3-NLCMO was ~120 mA h g^{-1}, even at 700 mA g^{-1}, which is ~58 % of the capacity measured at 15 mA g^{-1}. From a cycling performance point of view, Fig. 2(c) shows that the capacity of P3-NLCMO was retained at ~90% compared to its initial capacity after 100 cycles at 300 mA g^{-1}, with the high Coulombic efficiency of above 99%. Moreover, it is verified that the morphology of P3-NLCMO electrode was well retained after prolonged cycling and there are no noticeably large cracks in the as-prepared and 100-cycled P3-NLCMO electrodes, through the SEM analyses (Fig. S4).

To theoretically understand the P3-type layered oxide, we performed first-principles calculations based on the structural information verified by Riveted refinement and generated various Na/vacancy configurations by varying the vacancy content in $Na_x[Li_{0.1}Cu_{0.2}Mn_{0.7}]O_2$, using a cluster-assisted statistical mechanisms (CASM) software [42]. As shown in Fig. 2(d), we calculated the formation energies for various configurations of $Na_x[Li_{0.1}Cu_{0.2}Mn_{0.7}]O_2$ and arranged the data using a convex hull plot. The theoretical redox potentials of $Na_x[Li_{0.1}Cu_{0.2}Mn_{0.7}]O_2$ were calculated using the following equation:

$$V = -\frac{E[Na_{x_2}[Li_{0.1}Cu_{0.2}Mn_{0.7}]O_2] - E[Na_{x_1}[Li_{0.1}Cu_{0.2}Mn_{0.7}]O_2] - (x_2 - x_1)E[Na]}{(x_2 - x_1)F} \quad (1)$$

where *V* is the average redox potential between the Na ion content in $Na_x[Li_{0.1}Cu_{0.2}Mn_{0.7}]O_2$ ($x_1 \leq x \leq x_2$), and $E[Na_x[Li_{0.1}Cu_{0.2}Mn_{0.7}]O_2]$ is the most stable formation energy for each $Na_x[Li_{0.1}Cu_{0.2}Mn_{0.7}]O_2$ configuration. Here, *E*[Na] refers to the chemical potential of the Na metal, and *F* is the Faraday constant. The calculated voltages reveal

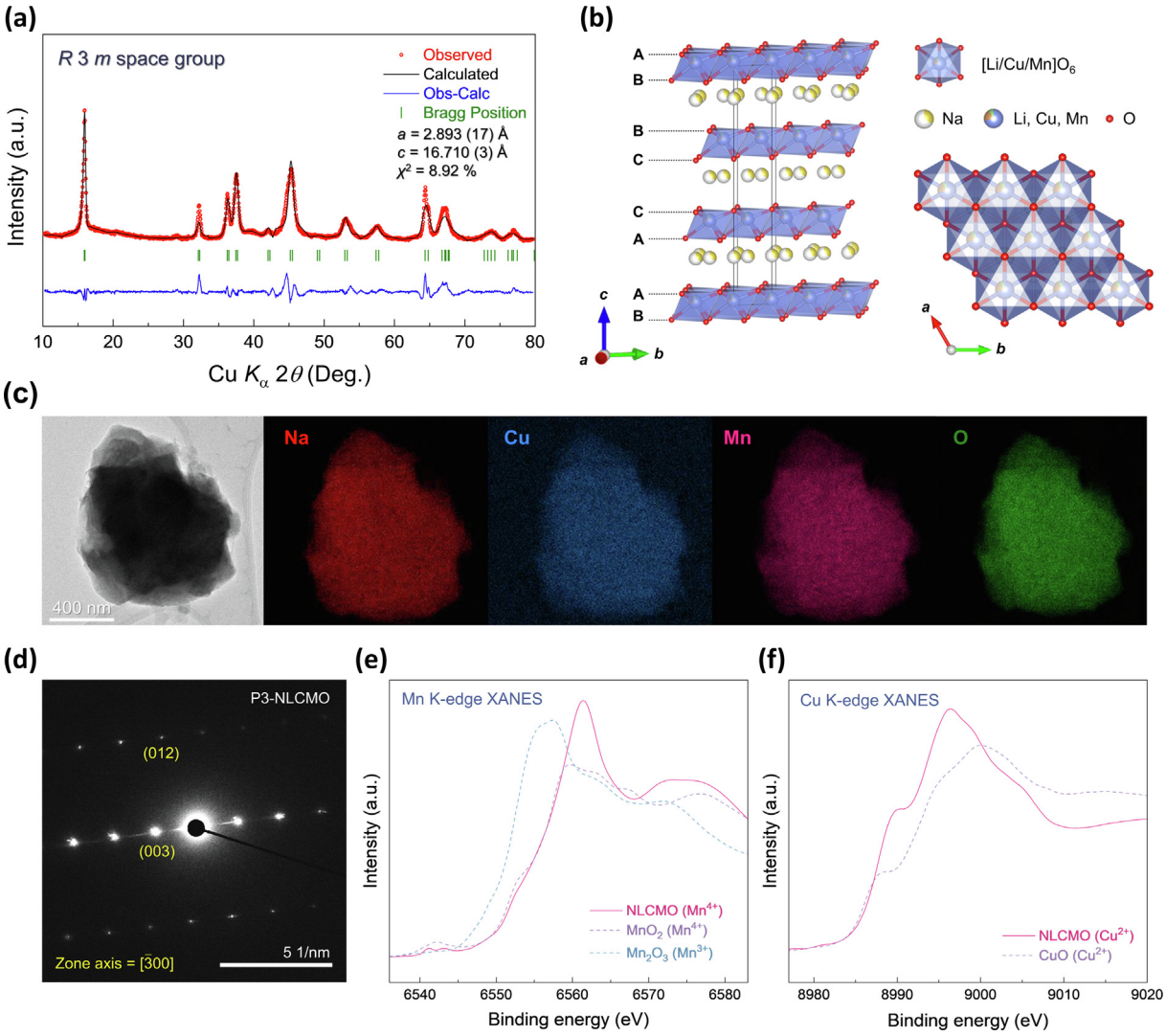

Fig. 1. (a) Rietveld refinement of XRD pattern (R_P = 7.69 %, R_I = 8.12 %, R_F = 6.31 %, and χ^2 = 8.92 %) and (b) crystal structures of P3-$Na_{0.7}[Li_{0.1}Cu_{0.2}Mn_{0.7}]O_2$. (c) TEM-EDS mapping and (d) SAED patterns of P3-$Na_{0.7}[Li_{0.1}Cu_{0.2}Mn_{0.7}]O_2$. (e) Mn and (f) Cu K-edge of P3-$Na_{0.7}[Li_{0.1}Cu_{0.2}Mn_{0.7}]O_2$ pristine electrode.

that more than ~0.8 mol Na^+ can be (de)intercalated from the host cathode in the available voltage range for SIBs, and the results are consistent with the experimentally measured charge/discharge curve at 15 mA g^{-1}, as shown in Fig. 2(e).

3.3. Unexpected merit by Li displacement to enhance the structural stability during OR

As shown in Fig. 2(d), we compared the thermodynamic phase stabilities of P3-$Na_x[Li_{0.1}Cu_{0.2}Mn_{0.7}]O_2$ and O3-$Na_x[Li_{0.1}Cu_{0.2}Mn_{0.7}]O_2$ at x = 0 and 0.25, using first-principles calculations. Interestingly, the P3-type phase was more stable than the O3-type phase, even after most of the Na^+ had deintercalated from the structure. This implies that there is a negligible phase transition of P3-O3″ in the oxide cathode during charging/discharging, unlike for other P3-type Na cathodes [34,47,48]. To demonstrate the predicted phase stability upon charging and discharging, we performed *operando* XRD analyses in the voltage window of 1.5–4.4 V, as shown in Fig. 3(a). Upon charging to 4.4 V, the (003) and (006) XRD peaks successively shifted toward a lower 2θ angle, indicating elongation of the interlayer distance along the *c*-axis. In contrast, the (101) and (012) XRD peaks shifted toward higher 2θ angles, indicating the shrinkage of the adjacent TM layers. The expansion of the *c*-axis originates from the increase in electrostatic repulsion between oxygen ions by Na^+ deintercalation [49,50]. In particular, the (003) and (006) XRD peaks were retained during charging to 4.4 V, and no new XRD peaks related to the O3-type phase were observed. These results reveal that P3-NLCMO is not favorable for the well-known phase transition of P3-O3″, even though its phase stability is still observed in the oxygen redox region. Generally, the P3-O3″ phase transition is attributed to the gliding of TM layers during deintercalation/intercalation process in the high-voltage region, which leads to the slight changes in TM interlayer distance through the electrostatic attraction and repulsion. The (003) XRD peak shifts to higher angle, suggesting the formation of a new hexagonal O3″ phase characterized by a highly faulted layered structure with significant peak broadening [25,51]. To examine the detailed structural variation of the oxide cathode, its lattice parameters were investigated via the Rietveld refinement of the operando XRD patterns during Na^+ de/intercalation, as shown in Fig. 3(b). Upon charging to 4.4 V, the variation of *a* and *c*-lattice parameters was only ~1.52% and ~1.12%, respectively, corresponding to the subtle decreased interlayer spacing. Its value is smaller than those of other reported P3-type oxide cathodes exhibiting P3-O3″ phase transition [43,47]. Furthermore, a small structural change occurred under the oxygen redox reaction, which is similar to the volume

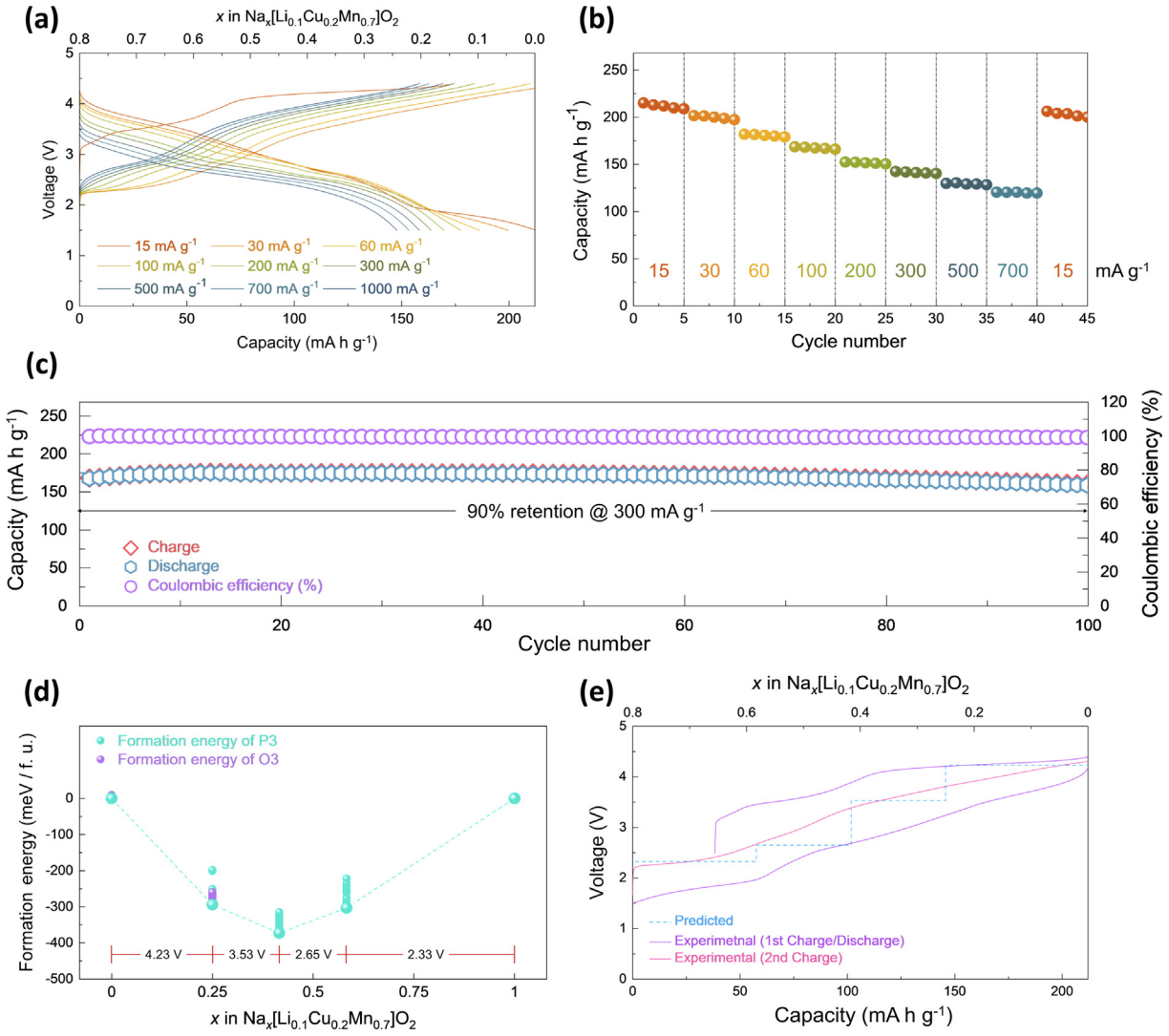

Fig. 2. (a) Charge/discharge profiles of P3-$Na_{0.7}[Li_{0.1}Cu_{0.2}Mn_{0.7}]O_2$ in the voltage range of 1.5–4.4 V at various discharge current densities and a charge current density of 15 mA g^{-1}. (b) Rate capability of P3-$Na_{0.7}[Li_{0.1}Cu_{0.2}Mn_{0.7}]O_2$. (c) Cycle performance of P3-$Na_{0.7}[Li_{0.1}Cu_{0.2}Mn_{0.7}]O_2$ at 300 mA g^{-1} over 100 cycles in the voltage range of 1.5–4.4 V (vs. Na^+/Na). (d) Convex-hull plot for formation energy of $Na_{1-x}[Li_{0.1}Cu_{0.2}Mn_{0.7}]O_2$ configurations ($0 \leq x \leq 1$) with theoretical voltage. (e) Comparison of theoretical voltage prediction of P3-$Na_{0.7}[Li_{0.1}Cu_{0.2}Mn_{0.7}]O_2$ and its experimentally measured charge/discharge profiles at 15 mA g^{-1}.

variation result. Unlike the fact that a large Na ionic radius triggers a large volume contraction and expansion upon cycling, which results in a decrease in capacity retention [52,53], the analyzed results show direct evidence in terms of a structural stability point of view. That is, mitigating the structural change during (de) oxidation enables outstanding cycle performance (shown in Fig. 2c). Therefore, the morphology and crystal structure of P3-NLCMO were well retained even after 100 cycles of the high-voltage charging process based on the anionic redox reaction (Figs. S4 and S5). In addition, we prepared P3-$Na_{0.7}[Li_{0.2}Cu_{0.1}Mn_{0.7}]O_2$ and measured its cyclability. In Fig. S6, P3-$Na_{0.7}[Li_{0.2}Cu_{0.1}Mn_{0.7}]O_2$ has the P3-type phase with the *R*3*m* space group, similar with P3-NLCMO. Table S3 indicates the detailed structural information of P3-$Na_{0.7}[Li_{0.2}Cu_{0.1}Mn_{0.7}]O_2$. It was verified that P3-$Na_{0.7}[Li_{0.2}Cu_{0.1}Mn_{0.7}]O_2$ exhibits a capacity retention of ~74% after 100 cycles at 300 mA g^{-1} with a high coulombic efficiency of above 99% (Fig. S7). Since oxygen redox is more dominantly participated in P3-$Na_{0.7}[Li_{0.2}Cu_{0.1}Mn_{0.7}]O_2$ during charge/discharge than P3-NLCMO, more large local structural change by oxygen redox is occurred at P3-$Na_{0.7}[Li_{0.2}Cu_{0.1}Mn_{0.7}]O_2$ than P3-NLCMO, which leads to better cyclability of P3-NLCMO than P3-$Na_{0.7}[Li_{0.2}Cu_{0.1}Mn_{0.7}]O_2$.

Taking into consideration that the phase transition from P- to O-type layered oxides plays a crucial role in facilitating Li migration into the Na layer, the suppression of the P3-O3″ phase transition at P3-NLCMO holds significance from a Li local structure perspective. Previous studies have reported Li ions stably occupy octahedral sites [32,54], while they are not preferential to prismatic sites. This observation can be explained by their site energies [7]. Since P3-NLCMO maintained its pristine structure throughout the electrochemical cycling, the energies of Li ions located in the TM layer and Na layer were compared for the Na-deficient P3 structure. Through first-principles calculation (Fig. 3c), Li ions situated in the Na layer exhibited relative site energy value of 2208.29 meV. It was verified that existence of Li ions in TM layer is more thermodynamically stable than that in Na layer, suggesting that the Li ions are more likely to locate in the energetically favorable TM layer. The octahedral and prismatic sites are similar in that they are both coordinated with six oxygen ions; however, the stacking sequence of oxygen atoms and the size of the polyhedron differ, with prismatic sites in the Na-ion layer being relatively lager to the octahedral sites in the TM layer. Since Li ions have a relatively small ionic radius, it is thermodynamically unstable when located in prismatic sites due to the large distance from oxygen

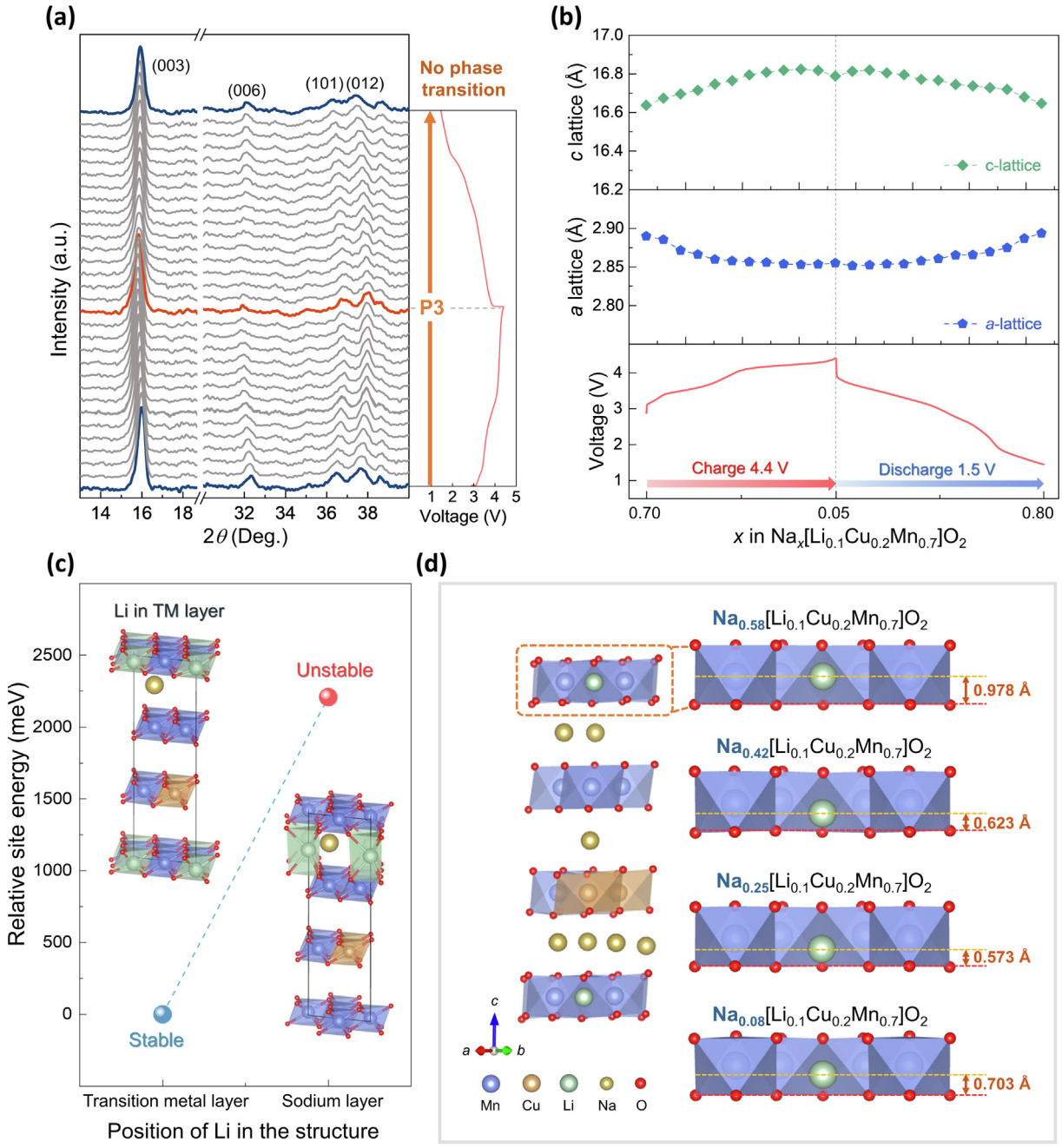

Fig. 3. (a) Ex-situ magnified view of operando XRD patterns of P3-Na$_{0.7}$[Li$_{0.1}$Cu$_{0.2}$Mn$_{0.7}$]O$_2$ during charge/discharge. (b) The variations of lattice parameters *a* and *c*, which are calculated from the operando XRD results of Na$_{0.7}$[Li$_{0.1}$Cu$_{0.2}$Mn$_{0.7}$]O$_2$ in the structure during charge/discharge. (c) Comparison of relative site energy of Li in transition-metal and sodium layers. (d) The schematics of the Li$^+$ displacement in the TM layers and change in calculated *c*-axis lattice parameters on various P3-Na$_x$[Li$_{0.1}$Cu$_{0.2}$Mn$_{0.7}$]O$_2$ compositions ($0 \leq x \leq 1$).

[54]. Additionally, it was verified that the theoretical redox potential on Li$^+$ deintercalation in the fully Na$^+$ deintercalated P3-Na$_0$[Li$_{0.1}$Cu$_{0.2}$Mn$_{0.7}$]O$_2$ is approximately 6.34 V (vs. Na$^+$/Na) (Fig. S8). This potential value falls outside the available voltage range for SIB systems. These results indicate the difficulty of Li$^+$ deintercalation from the P3-type host material, even after charging it to the high-voltage region. For direct understanding, we performed ICP-AES measurements to measure the Li content in P3-NLCMO after prolonged cycling. As shown in Table S4, most of the Li remained in the cathode after 10 cycles, which reinforces the theoretical calculation results.

To obtain a deeper understanding of the Li ion behavior in the TM layer upon charging, we investigated the local structure of LiO$_6$ in Na$_x$[Li$_{0.1}$Cu$_{0.2}$Mn$_{0.7}$]O$_2$ as a function of Na content, and its values denoted as "Li displacement" are summarized in Fig. 3(d). For a better understanding, the captured local slab and the average positions of the Li ions were plotted at various Na contents in Na$_x$[Li$_{0.1}$Cu$_{0.2}$Mn$_{0.7}$]O$_2$, and the displacement was evaluated based on the distance from the average oxygen position. The *c* lattice parameter increased and then decreased, whereas the Li displacement showed an opposite pathway during Na$^+$ deintercalation (Table S5). These local structural results indicate that the Li ion is reversibly displaced depending on the structural contraction and expansion of the crystal framework without extraction. Combined with the stepwise redox reaction, it is anticipated that the intriguing local structure mechanism plays a supportive role in

suppressing the structural changes of P3-NLCMO and forming dimers of oxygen ions in deeply charged states, and the importance of Li ion is emphasized in similar Mn-based cathodes exhibiting OR [30]. In general, OR reactions enable additional capacity implementation in the high-voltage region, allowing for the storage of a higher energy density compared to conventional charge/discharge mechanisms. However, the contraction of interlayer O—O bonding caused by OR induces the distortion of TMO_6 octahedra, which leads to the gliding of the oxygen layers and the subsequent occurrence of P—O phase transition. In P3-NLCMO, the Li displacement in LiO_6 octahedra during Na^+ de/intercalation was verified to be slightly along with c-axis direction, which can contribute to alleviate the elongation of TM–O bonding. Thus, the difficulty for the coordinated gliding of oxygen ions can be increased by the Li displacement, which can suppress the large structural change such as phase transition of P3-O3" and enable the outstanding cycle performance of P3-$Na_{0.7}[Li_{0.1}Cu_{0.2}Mn_{0.7}]O_2$. Furthermore, it was confirmed that the cyclability of anionic-redox-based P3-NLCMO was better than that of other P3-type Na-layered oxide cathode materials (Fig. 4) [32,34,47,55–58]. Despite the differences in the electrochemical testing conditions among the samples (Table S6), this comparison revealed that P3-NLCMO can deliver high competitiveness as a promising cathode material for SIBs. Interestingly, it was verified that 0.2 mol Li-substituted P3-$Na_{0.6}[Li_{0.2}Mn_{0.8}]O_2$ exhibits a capacity degradation of ~34% after 60 cycles at 200 mA g^{-1}, which is attributed to the occurrence of stacking faults [32]. Moreover, in the case of 0.25 mol Li-substituted P2-$Na_{0.75}[Li_{0.25}Mn_{0.75}]O_2$, it experiences severe structural instability induced by redox-active oxygen sites near Li ions, which results in phase transition and poor cyclability [30,45]. These results imply that the too much Li contents in the transition metal (TM) site can lead to excessive oxygen redox reactions during charge/discharge and significant structural changes, such as phase transitions. Consequently, it is crucial to establish the appropriate structural conditions by optimizing the lithium-substitution content and elemental combination in the TM site in order to facilitate stable oxygen redox processes without severe structural changes.

3.4. Stepwise redox mechanism for harnessing the full potential of OR

Although OR has been acknowledged as an intriguing paradigm for overcoming the limitations of SIBs and LIBs, the formation of an O—O dimer over the oxide frameworks is considered an inevitable hurdle upon charging. This dimerization degrades the anionic capacity and induces its hysteresis after the first activation. In light of this, modulating the oxygen capacity was highlighted as a rational method for harnessing full potential of the OR upon cycling. These considerations motivated an in-depth investigation of the stepwise redox mechanism based on Cu and O ions for the layered oxide cathode, and it is anticipated that the cation plays an assisting role in avoiding harsh environmental conditions in the deeply charged state. To experimentally demonstrate the redox reactions of P3-NLCMO upon charging, we performed the synchrotron-based ex-situ X-ray absorption near-edge structure (XANES).

Fig. 5(a) shows the Mn K-edge XAENS spectra of P3-NLCMO with different charge states, showing that there is no significant shift of the Mn K-edge during charging to 4.4 V. This result indicates that further oxidation of Mn^{4+} did not occur during Na^+ deintercalation from the host cathode. In addition, it was demonstrated that the Mn K-edge XANES was shifted toward lower energy level upon discharging to 1.5 V, which indicate the occurrence of Mn^{3+}/Mn^{4+} redox reaction in P3-NLCMO during discharge. These results are also well matched with the previous research [59,60]. Thus, it could be confirmed that the reduction peak at around 1.8 V (Fig. S3) is attributed to the Mn^{3+}/Mn^{4+} redox reaction of P3-

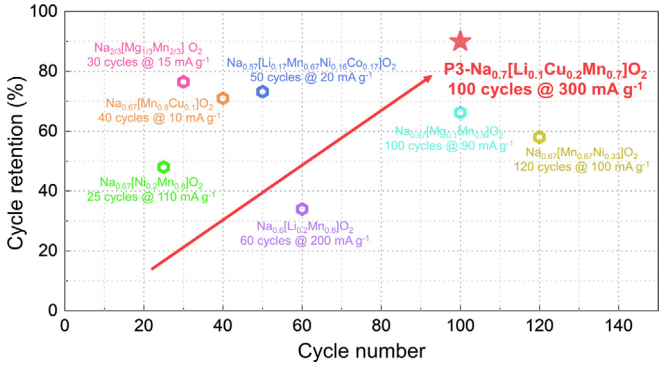

Fig. 4. Comparison of the cycle performance of P3-$Na_{0.7}[Li_{0.1}Cu_{0.2}Mn_{0.7}]O_2$ and other P3-type cathode materials for Na-ion batteries.

NLCMO. In terms of the Cu K-edge XAENS spectra of P3-NLCMO (Fig. 5b), it was demonstrated that P3-$Na_{0.7}[Li_{0.1}Cu_{0.2}Mn_{0.7}]O_2$ consists of Cu^{2+} cation like CuO. During charge, Cu K-edge was shifted toward higher energy level during charge, which implies occurrence of Cu^{2+}/Cu^{3+} redox reaction in P3-$Na_{0.7}[Li_{0.1}Cu_{0.2}Mn_{0.7}]O_2$. This result is well matched with the several previous research [33,60]. In addition, we performed the ex-situ EXAFS analyses to verify the local structural change during charge/discharge. As shown in Fig. S9, it was verified that Mn—O and Cu—O bond distances were shortened from 1.41 to 1.38 Å and from 1.32 to 1.29 Å, respectively, upon charging. After discharge, they almost returned to their as-prepared state. Furthermore, the peak shapes of EXAFS spectra were well retained during charge/discharge. These results indicate that there is no severe structural distortion on the local environments of TM-O octahedral in $Na_x[Li_{0.1}Cu_{0.2}Mn_{0.7}]O_2$ during the cationic and anionic redox reactions. To demonstrate the OR in the P3-type cathode model, we performed ex-situ O K-edge soft X-ray absorption spectroscopy (sXAS) in the total fluorescence yield (TFY) mode, as shown in Fig. 5(c). The pre-edge peaks of the O K-edge correspond to unoccupied TM($3d$) – O($2p$) t_{2g} and e_g hybridized orbitals. During charging to 4.1 V, the intensities of the oxygen pre-edge peaks at ~529 and ~531 eV increased. These results revealed the creation of the hole state in the TM($3d$) – O($2p$) hybridized orbitals and confirmed the Cu^{2+}/Cu^{3+} redox reaction. Moreover, the intensity at ~530.4 eV evolved after further charging to 4.4 V by comparing the intensities of each O K-edge sXAS spectrum (see the lower panel of Fig. 3d). Considering that the increase in the intensity at ~530.4 eV results from the localized features of the oxidized oxygen states [7,61–64], the XAS observations of the oxygen ions confirm the OR occurrence in P3-NLCMO. Furthermore, we performed ex-situ X-ray photoelectron spectroscopy (XPS) analysis of the O($1s$) spectra, as shown in Fig. S10. The peak corresponding to the peroxo-like species appeared at ~530.4 eV after charging to 4.4 V [8,65]. These ex-situ O K-edge sXAS and O($1s$) XPS results validate the stepwise charge-compensation mechanism based on oxygen ions in P3-NLCMO upon Na^+ deintercalation.

To understand the OR mechanism in detail, we investigated the electronic structure changes of cations and anions upon charging the oxide cathode. Fig. 5(d and e) show the theoretical DOSs and visualized electron and hole densities at x = 0.58, 0.42, and 0 in P3-$Na_x[Li_{0.1}Cu_{0.2}Mn_{0.7}]O_2$. During Na^+ deintercalation from Na0.58 phase to Na0.42 phase, the hybridized electron density of Cu($3d$) – O($2p$) was changed to the hole density, which indicates occurrence of the Cu^{2+}/Cu^{3+} redox reaction and the Cu-redox-resulted OR. In addition, unhybridized O($2p$) electron densities over the entire crystal framework were activated at x = 0.42 in P3-$Na_x[Li_{0.1}Cu_{0.2}Mn_{0.7}]O_2$, deeming them as the sole factor for the

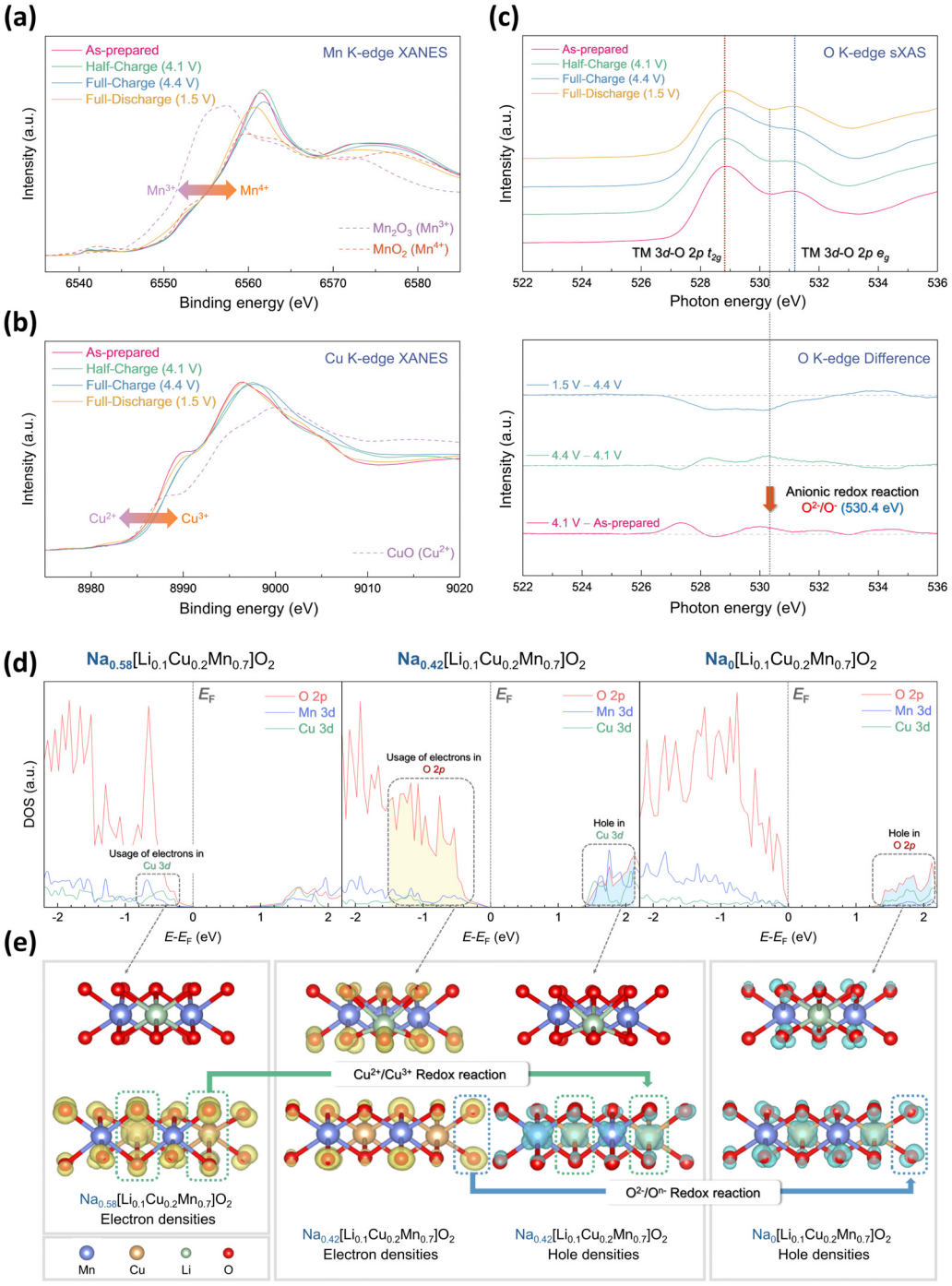

Fig. 5. Ex-situ analyses of P3-$Na_{0.7}[Li_{0.1}Cu_{0.2}Mn_{0.7}]O_2$: (a) Mn and (b) Cu K-edge XANES spectra. (c) O K-edge sXAS spectra and difference spectra (lower panel) obtained by subtracting O K-edge sXAS spectra. (d) pDOS of Mn 3*d*, Cu 3*d* and O 2*p* of $Na_x[Li_{0.1}Cu_{0.2}Mn_{0.7}]O_2$ ($0 \leq x \leq 1$). (e) Visualized pDOS on Mn, Cu 3*d* and O 2*p* orbitals on $Na_{0.58}[Li_{0.1}Cu_{0.2}Mn_{0.7}]O_2$, $Na_{0.42}[Li_{0.1}Cu_{0.2}Mn_{0.7}]O_2$ and $Na_0[Li_{0.1}Cu_{0.2}Mn_{0.7}]O_2$: electron density (yellow) and hole density (blue).

charge compensation mechanism upon further Na^+ deintercalation. And then, during further Na^+ deintercalation to Na0 phase, only the electron density of O 2*p* orbital was changed to the hole density, which indicates the OR occurrence in P3-$Na_x[Li_{0.1}Cu_{0.2}Mn_{0.7}]O_2$. The intriguing redox reaction was also understood by comparing the effective charges of cations and anions upon charging in the P3-type oxide, and their values were calculated based on Bader charge analysis (Fig. S11). The effective charge of the Mn ion changed negligibly over the full Na content, whereas that of the Cu ion significantly increased from x = 0.58 to 0.42 in $Na_x[Li_{0.1}Cu_{0.2}Mn_{0.7}]O_2$. From the oxygen point of view, the charge value simultaneously increases in the same x range because of the hybridized electrons of Cu(3*d*) – O(2*p*). Further Na^+ deintercalation leads to a linear increase in the oxygen effective charge compared to the slight changes in Mn and Cu ions, which consistently explains the oxygen redox in P3-NLCMO.

4. Conclusions

We demonstrated that the co-existence of Cu and Li cations can result in the outstanding electrochemical performances of P3-NLCMO as the promising cathode for SIBs. During charge/discharge

process, P3-NLCMO delivered a specific capacity of ~212 mA h g^{-1} at a current density of 15 mA g^{-1}. Even at 300 mA g^{-1} for 100 cycles, the specific capacity was retained up to ~90% of the theoretical capacity with a high Coulombic efficiency of above 99%, implying the outstanding cycle performance with the stable OR. *Operando* XRD observations and first-principles calculations clearly revealed the suppression of the P3-O3″ phase transition under the small structural variation in the OR region upon (dis)charging, and Li displacement was deemed as a supportive function in restraining the phase transition from a local structural point of view. Moreover, the various redox reactions of Cu, Mn and O ions occurred during charge/discharge were confirmed through ex-situ XANES and sXAS analyses. The first-principles calculation results on theoretical DOSs clearly showed the results of electron and hole densities elucidated that the hybridized Cu($3d$) − O($2p$) electron played a dominant role in compensating the charge imbalance caused by Na^+ deintercalation, and oxygen oxidation was identified as a major factor for the remaining charge compensation. Our well-arranged understanding of the reaction mechanism offers an effective direction for facilitating sustainable OR, and the synergetic concept is expected to be global for high-energy–density Na oxide cathodes.

Declaration of competing interest

The authors declare that they have no known competing financial interests or personal relationships that could have appeared to influence the work reported in this paper.

Acknowledgments

This research was supported by the National Research Foundation of Korea grant funded by the Korea government (NRF-2021R1A2C1014280) and the Fundamental Research Program of the Korea Institute of Material Science (PNK9370).

Appendix A. Supplementary material

Supplementary data to this article can be found online at https://doi.org/10.1016/j.jechem.2023.06.009.

References

[1] M. Armand, J.-M. Tarascon, Nature 451 (2008) 652–657.
[2] D. Larcher, J.-M. Tarascon, Nat. Chem. 7 (2015) 19–29.
[3] B. Scrosati, J. Garche, J. Power Sources 195 (2010) 2419–2430.
[4] A. Manthiram, JOM 49 (1997) 43–46.
[5] T. Kim, W. Choi, H.-C. Shin, J.-Y. Choi, J.M. Kim, M.-S. Park, W.-S. Yoon, J. Electrochem. Sci. Technol. 11 (2020) 14–25.
[6] S.-W. Kim, D.-H. Seo, X. Ma, G. Ceder, K. Kang, Adv. Energy Mater. 2 (2012) 710–721.
[7] S. Lee, W. Ko, H. Park, Y. Lee, J. Kang, J. Ahn, S. Lee, E. Sim, K. Ihm, K.-Y. Park, J. Kim, Chem. Eng. J. 451 (2023).
[8] S. Lee, J. Kang, M.-K. Cho, H. Park, W. Ko, Y. Lee, J. Ahn, S. Lee, E. Sim, K. Ihm, J. Hong, H. Kim, J. Kim, Appl. Phys. Rev. 9 (2022).
[9] J. Kang, J. Ahn, H. Park, W. Ko, Y. Lee, S. Lee, S. Lee, S. Jung, J. Kim, Adv. Funct. Mater. 32 (2022) 2201816.
[10] H. Park, Y. Lee, M.-K. Cho, J. Kang, W. Ko, Y.H. Jung, T.-Y. Jeon, J. Hong, H. Kim, S.-T. Myung, J. Kim, Energy Environ. Sci. 14 (2021) 1469–1479.
[11] C. Delmas, Adv. Energy Mater. 8 (2018) 1703137.
[12] T. Liu, Y. Zhang, Z. Jiang, X. Zeng, J. Ji, Z. Li, X. Gao, M. Sun, Z. Lin, M. Ling, J. Zheng, C. Liang, Energy Environ. Sci. 12 (2019) 1512–1533.
[13] W. Ko, M. Cho, J. Kang, H. Park, J. Ahn, Y. Lee, S. Lee, S. Lee, K. Heo, J. Hong, J. Yoo, J. Kim, Energy Storage Mater. 46 (2022) 289–299.
[14] N. Yabuuchi, K. Kubota, M. Dahbi, S. Komaba, Chem. Rev. 114 (2014) 11636–11682.
[15] K. Kubota, N. Yabuuchi, H. Yoshida, M. Dahbi, S. Komaba, MRS Bull. 39 (2014) 416–422.
[16] D. Zhou, D. Ning, J. Wang, J. Liu, G. Zhang, Y. Xiao, J. Zheng, Y. Li, J. Li, X. Liu, J. Energy Chem. 77 (2023) 479–486.
[17] J. Wang, D. Zhou, X. He, L. Zhang, X. Cao, D. Ning, B. Yan, X. Qi, J. Li, V. Murzin, E. Paillard, X. Liu, G. Schumacher, M. Winter, J. Li, A.C.S. Appl, Mater. Interfaces 12 (2020) 5017–5024.
[18] M. Saubanère, E. McCalla, J.-M. Tarascon, M.-L. Doublet, Energy Environ. Sci. 9 (2016) 984–991.
[19] M. Kim, H. Kim, M. Cho, D. Kim, J. Mater. Chem. A 9 (2021) 15179–15187.
[20] W.E. Gent, I.I. Abate, W. Yang, L.F. Nazar, W.C. Chueh, Joule 4 (2020) 1369–1397.
[21] J. Hong, W.E. Gent, P. Xiao, K. Lim, D.-H. Seo, J. Wu, P.M. Csernica, C.J. Takacs, D. Nordlund, C.-J. Sun, K.H. Stone, D. Passarello, W. Yang, D. Prendergast, G. Ceder, M.F. Toney, W.C. Chueh, Nat. Mater. 18 (2019) 256–265.
[22] S.M. Kang, D. Kim, K. Lee, M. Kim, A. Jin, J. Park, C. Ahn, T.-Y. Jeon, Y.H. Jung, S.-H. Yu, J. Mun, Y. Sung, Adv. Sci. 7 (2020) 2001263.
[23] D. Kwon, S.J. Park, J. Lee, S. Park, S.H. Yu, D. Kim, Adv. Sci. 10 (2023) 2206367.
[24] K. Du, J. Zhu, G. Hu, H. Gao, Y. Li, J.B. Goodenough, Energy Environ. Sci. 9 (2016) 2575–2577.
[25] S. Komaba, N. Yabuuchi, T. Nakayama, A. Ogata, T. Ishikawa, I. Nakai, Inorg. Chem. 51 (2012) 6211–6220.
[26] N. Tapia-Ruiz, W.M. Dose, N. Sharma, H. Chen, J. Heath, J.W. Somerville, U. Maitra, M.S. Islam, P.G. Bruce, Energy Environ. Sci. 11 (2018) 1470–1479.
[27] R.A. House, U. Maitra, M.A. Pérez-Osorio, J.G. Lozano, L. Jin, J.W. Somerville, L.C. Duda, A. Nag, A. Walters, K.-J. Zhou, M.R. Roberts, P.G. Bruce, Nature 577 (2020) 502–508.
[28] J. Lee, J. Kim, S. Park, D. Kim, Energy Storage Mater. 54 (2023) 330–338.
[29] J. Lee, S. Park, G. Choi, D. Kwon, J. Kim, H. Kim, M. Cho, D. Kim, Adv. Energy Mater. 12 (2022) 2201319.
[30] S. Koo, I.-H. Ko, J. Lee, S.-M. Kang, S.-H. Yu, D. Kim, ChemElectroChem 8 (2021) 1464–1472.
[31] M. Luo, S. Zheng, J. Wu, K. Zhou, W. Zuo, M. Feng, H. He, R. Liu, J. Zhu, G. Zhao, S. Chen, W. Yang, Z. Peng, Q. Wu, Y. Yang, J. Mater. Chem. A 8 (2020) 5115–5127.
[32] X. Rong, J. Liu, E. Hu, Y. Liu, Y. Wang, J. Wu, X. Yu, K. Page, Y.-S. Hu, W. Yang, H. Li, X.-Q. Yang, L. Chen, X. Huang, Joule 2 (2018) 125–140.
[33] C. Cheng, C. Chen, S. Chu, H. Hu, T. Yan, X. Xia, X. Feng, J. Guo, D. Sun, J. Wu, S. Guo, L. Zhang, Adv. Mater. 34 (2022) 2201152.
[34] S.F. Linnell, A.G. Manche, Y. Liao, M. Hirsbrunner, S. Imada, A.B. Naden, J.T.S. Irvine, L.C. Duda, A.R. Armstrong, J. Phys. Energy 4 (2022).
[35] J. Rodríguez-Carvajal, Phys. B Condens. Matter 192 (1993) 55–69.
[36] B. Ravel, M. Newville, Phys. Scr. 115 (2005) 1007.
[37] G. Kresse, J. Furthmüller, Comput. Mater. Sci. 6 (1996) 15–50.
[38] P.E. Blöchl, Phys. Rev. B 50 (1994) 17953–17979.
[39] J.P. Perdew, K. Burke, M. Ernzerhof, Phys. Rev. Lett. 77 (1996) 3865–3868.
[40] A. Jain, G. Hautier, S.P. Ong, C.J. Moore, C.C. Fischer, K.A. Persson, G. Ceder, Phys. Rev. B 84 (2011).
[41] J. Heyd, G.E. Scuseria, M. Ernzerhof, J. Chem. Phys. 118 (2003) 8207–8215.
[42] A. Van der Ven, J.C. Thomas, Q. Xu, J. Bhattacharya, Math. Comput. Simul. 80 (2010) 1393–1410.
[43] Y. Shi, Z. Zhang, P. Jiang, A. Gao, K. Li, Q. Zhang, Y. Sun, X. Lu, D. Cao, X. Lu, Energy Storage Mater. 37 (2021) 354–362.
[44] X. Chen, X. Zhou, M. Hu, J. Liang, D. Wu, J. Wei, Z. Zhou, J. Mater. Chem. A 3 (2015) 20708–20714.
[45] L. Yang, X. Li, X. Ma, S. Xiong, P. Liu, Y. Tang, S. Cheng, Y.-Y. Hu, M. Liu, H. Chen, J. Power Sources 381 (2018) 171–180.
[46] X. Rong, E. Hu, Y. Lu, F. Meng, C. Zhao, X. Wang, Q. Zhang, X. Yu, L. Gu, Y.-S. Hu, H. Li, X. Huang, X.-Q. Yang, C. Delmas, L. Chen, Joule 3 (2019) 503–517.
[47] B. Song, E. Hu, J. Liu, Y. Zhang, X.-Q. Yang, J. Nanda, A. Huq, K. Page, J. Mater. Chem. A 7 (2019) 1491–1498.
[48] T. Risthaus, L. Chen, J. Wang, J. Li, D. Zhou, L. Zhang, D. Ning, X. Cao, X. Zhang, G. Schumacher, M. Winter, E. Paillard, J. Li, Chem. Mater. 31 (2019) 5376–5383.
[49] Y. Huang, Y. Dong, S. Li, J. Lee, C. Wang, Z. Zhu, W. Xue, Y. Li, J. Li, Adv. Enegry Mater. 11 (2020).
[50] P. Ge, Solid State Ionics 28–30 (1988) 1172–1175.
[51] X. Li, D. Wu, Y.-N. Zhou, L. Liu, X.-Q. Yang, G. Ceder, Electrochem. Commun. 49 (2014) 51–54.
[52] J.-M. Tarascon, Joule 4 (2020) 1616–1620.
[53] A. Mukhopadhyay, B.W. Sheldon, Prog. Mater. Sci. 63 (2014) 58–116.
[54] D. Eum, B. Kim, J.-H. Song, H. Park, H.-Y. Jang, S.J. Kim, S.-P. Cho, M.H. Lee, J.H. Heo, J. Park, Y. Ko, S.K. Park, J. Kim, K. Oh, D.-H. Kim, S.J. Kang, K. Kang, Nat. Mater. 21 (2022) 664–672.
[55] E.J. Kim, L.A. Ma, L.C. Duda, D.M. Pickup, A.V. Chadwick, R. Younesi, J.T.S. Irvine, A. Robert Armstrong, ACS Appl. Energy Mater. 3 (2020) 184–191.
[56] B. Sambandam, M.H. Alfaruqi, S. Park, S. Lee, S. Kim, J. Lee, V. Mathew, J.-Y. Hwang, J. Kim, ACS Appl. Mater. Interfaces 13 (2021) 53877–53891.
[57] L. Zhang, J. Wang, J. Li, G. Schuck, M. Winter, G. Schumacher, J. Li, Nano Energy 70 (2020).
[58] Q. Huang, J. Liu, L. Zhang, S. Xu, L. Chen, P. Wang, D.G. Ivey, W. Wei, Nano Energy 44 (2018) 336–344.
[59] N. Yabuuchi, R. Hara, K. Kubota, J. Paulsen, S. Kumakura, S. Komaba, J. Mater. Chem. A 2 (2014) 16851–16855.
[60] P.-F. Wang, Y. Xiao, N. Piao, Q.-C. Wang, X. Ji, T. Jin, Y.-J. Guo, S. Liu, T. Deng, C. Cui, L. Chen, Y.-G. Guo, X.-Q. Yang, C. Wang, Nano Energy 69 (2020).

[61] J. Ahn, J. Kang, M.-K. Cho, H. Park, W. Ko, Y. Lee, H. Kim, Y.H. Jung, T.-Y. Jeon, H. Kim, W.-H. Ryu, J. Hong, J. Kim, Adv. Energy Mater. 11 (2021) 2102311.
[62] G. Assat, A. Iadecola, D. Foix, R. Dedryvère, J.-M. Tarascon, ACS Energy Lett. 3 (2018) 2721–2728.
[63] S. Roychoudhury, R. Qiao, Z. Zhuo, Q. Li, Y. Lyu, J. Kim, J. Liu, E. Lee, B.J. Polzin, J. Guo, S. Yan, Y. Hu, H. Li, D. Prendergast, W. Yang, Energy Environ. Mater. 4 (2021) 246–254.
[64] Y. Lee, H. Park, M. Cho, J. Ahn, W. Ko, J. Kang, Y.J. Choi, H. Kim, I. Park, W. Ryu, J. Hong, J. Kim, Adv. Funct. Mater. 32 (2022) 2204354.
[65] P.E. Pearce, A.J. Perez, G. Rousse, M. Saubanère, D. Batuk, D. Foix, E. McCalla, A. M. Abakumov, G. Van Tendeloo, M.-L. Doublet, J.-M. Tarascon, Nat. Mater. 16 (2017) 580–586.